Journal of Medical Robotics Research, Vol. 0, No. 0 (2016) 1–14

Fracture-directed Steerable Needles

Fan Yang[a,*], Mahdieh Babaiasl[a], John P. Swensen[a]

[a]*School of Mechanical and Materials Engineering, Washington State University, Pullman, WA 99164, USA*
E-mail: fan.yang6@wsu.edu

Steerable needles hold the promise of improving the accuracy of both therapies and biopsies as they are able to steer to a target location around obstructions, correct for disturbances, and account for movement of internal organs. However, their ability to make late-insertion corrections has always been limited by the lower bound on the attainable radius of curvature. This project involves a new class of steerable needle insertion where the objective is to first control the direction of tissue fracture with an inner stylet and later follow with the hollow needle. This method is shown to be able to achieve radius of curvature as low as 6.9 mm across a range of tissue stiffnesses and the radius of curvature is controllable from the lower bound up to a near infinite radius of curvature based on the stylet/needle step size. The approach of "fracture-directed" steerable needles indicates the promise of the technique for providing a tissue-agnostic method of achieving high steerability that can account for variability in tissues during a typical procedure and achieve radii of curvature unattainable through current bevel-tipped techniques. A variety of inner stylet geometries are investigated using tissue phantoms with multiple stiffnesses and discrete-step kinematic models of motion are derived heuristically from the experiments. The key finding presented is that it is the geometry of the stylet and the tuning of the bending stiffnesses of both the stylet and the tube, relative to the stiffness of the tissue, that allow for such small radius of curvature even in very soft tissues.

Keywords: continuum robot; medical robot; steerable needle; SEBS tissue

1. Introduction

Steerable needle research has shown the potential to improve outcomes in a variety of procedures from transoral access to the lung[1] to automated targeting in the breast[2] to MRI-compatible prostate intervention with steerable needles.[3] The potential method and applications of steerable needles are still very much in a nascent stage.[4]

However, the field of steerable needles has been dominated by the principle of using a beveled or pre-curved tip, or both, to create an asymmetric force at the tip of a needle and thus affecting the direction of tissue fracture as the needle is inserted.[5,6]

In the case of guide wires and sub-millimeter needle diameters, this asymmetric force is wholly dependent on the control surface in the case of bevel tips[7] or the angle, stiffness, and length of the pre-bend,[8] in conjunction with the stiffness of the tissue in which the needle tip is operating. This intrinsic dependence of both needle material, needle geometry, and tissue properties to cause a resulting curvature motivates the search for a new paradigm in steerable needles. This paper presents a class of "fracture-directed steerable needles", where the objective is to first control the direction of tissue fracture and then have the needle follow the fractured path. While the proposed method is one possible way of implementing fracture-directed steerable needles, the notion of fracture-directed steering promises the potential of radius of curvature and steerability currently unattainable with tip-steerable needles.

Figure 1 describes the principles of the stylet and tube form of fracture-directed steerable needles, where an inner stylet with a predefined geometry is first extended from the tube to fracture the tissue, after which the tube follows the stylet along the fracture direction.

The proposed method of fracture-directed needle steering consists of a straight outer elastic tube and an inner elastic wire stylet. This paper explores the effects of the pre-set shape of the inner stylet and the relative extension of the stylet from the tube on the achievable curvature of the needle in multiple tissue stiffnesses. A kinematic model relating the distance the inner stylet is inserted before following with the needle is derived and a linear relationship

---

[*] Fan Yang is with Washington State University (WSU), Pullman, WA 99164 USA (email: fan.yang6@wsu.edu).

between curvature, κ, and stylet insertion distance is presented. The achievable insertion radius is improved over existing pre-curved and bevel-tipped approaches and the low radius of curvature is demonstrated across a range of simulated tissue stiffnesses.

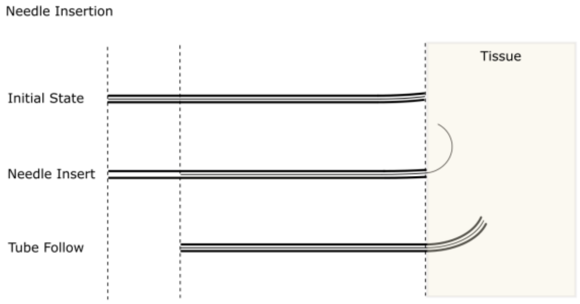

Fig. 1: Principle of fracture-directed steering. First the inner stylet is advanced, followed by the outer tube. The shape of the tissue fracture closely matches the geometry of the inner stylet. After the outer tube follows the inner stylet, the resulting tip position depends on the static equilibrium of the wire, tube, and tissue.

The proposed approach is not the only feasible method of fracture-directed steerable needles, but is a fundamental deviation from existing techniques in that the objective is first to control the direction of tissue fracture and then follow the fracture with the needle. The high curvature and lessened dependence on tissue stiffness demonstrated in this paper, and the relatively small deviation in terms of experimental apparatus from existing steering methods, provide the promise that fracture-directed steerable needles could fundamentally change how needle steering is accomplished in the future.

The majority of steerable needle approaches can be classified into categories of bevel-tipped steering, pre-bend steering, duty-cycle steering, external lateral manipulation, active cannulae (primarily for traversal of open spaces), and combinations of multiple modalities.[4,9] The bevel-tipped, pre-bend, and duty-cycle classes of steerable needles are all attempting to create an asymmetric force at the tip of the needle that will cause the tissue fracture to occur at an angle.[5,6,10] Of these types, duty-cycle steering is an adaptation of bevel-tipped steering where the relative rate of needle rotation to the insertion distance controls the curvature as a ratio from the zero duty cycle maximum curvature to the 100% duty cycle infinite curvature.[11]

Recent efforts have controlled the angle of a pre-bend with a fixed distal length using either tendons,[8] with application in liver ablations,[12] or an externally applied magnetic field,[13] with applications in deep brain stimulation. While able to achieve the best insertion radius to date among all methods of steerable needles, this approach still had the undesirable effect that any change in the angle at the tip of the needle, with the requisite forces to achieve tissue deformation, will necessarily cause large displacements in the tissue directly surrounding the tip. The magnitude of this deformation will depend on the fulcrum length of the distal portion beyond the actuated joint and the softness of the tissue. Duty-cycle methods also must account for the inherent torsional windup associated with twisting a long, super-elastic needle about the insertion axis.[14,15]

Another popular technique used for both bevel-tipped steerable needles and duty-cycle steerable needles has been to find ways to selectively reduce the bending stiffness of the steerable needle in one rotational degree of freedom. One approach has been to create notched needles that effectively reduce the bending stiffness in the plane of the notched section.[16] This is among a whole class of designs that attempt to selectively reduce the stiffness in a portion of the needle through creating thinner geometries along the length of the needle, often near the tip and sometimes with variable geometry.[12,17,18]

The method proposed in this paper is in close correlation with H. B. Gilbert *et al.*[19] and M. Neumann *et al.*[20] The main differences between these works and the method presented in this paper are the step method and the tuning between the tissue, tube, and wire.

The work presented in this paper is most closely related to very early steerable needle work by Okazawa *et al.*[21] where a pre-curved stylet is extended from a tube to create a controllable prebend. However, this method is still a variation of the pre-bend approach where the intent is to create an asymmetric force at the tip of the needle to try and change the direction of tissue fracture. This paper describes an alternate approach using a stylet and tube, where the stylet is extended from the tube while the tube is held fixed and then the tube follows while holding the stylet fixed. The approach results in a fundamentally different approach to steerable needles where we first control the direction of tissue fracture through the geometric design of the stylet, and simply follow the tissue fracture with the tube. In the latter portion of each step when the tube is following the channel cut by the stylet, the resultant shape of stylet, tube, and tissue channel can be computed in a manner similar to the active cannulae approach to open space traversal, where the tissue channel is treated as the outermost tube.[22,23]

2. Materials and Methods

With the general-purpose experimental apparatus for this stepped approach to fracture-directed steerable needles described, the remaining objectives of this paper are to evaluate the effects of the stylet geometry and the step size between stylet and tube on the insertion radius of the needle motion. As such, we first determine the allowable geometries of the Nitinol stylets that would result in strains that remain below the point of plastic deformation for both the stylets and the tubes when in the completely overlapped configuration. We have also developed transparent tissue phantoms that span a certain range of simulated tissue stiffnesses to evaluate the effectiveness of the approach using different needles inserted into multiple tissue stiffnesses.

2.1. *Tissue Preparation*

Two types of tissues are used for our experiments. The first category is Silicone Compound tissues consisting of Shore 10 Fast, Shore 10 Medium, Shore 20 Medium and Shore 00-50. Shore 00-50 is Platinum-Catalyzed Silicone. Except for Shore 00-50, all elastomers are High-Performance Platinum Cure Liquid Silicone compounds. Shore 20 Medium has the highest Shore A Hardness Scale 20A, Shore 10F and Shore 10M has the same Shore A Hardness, 10A, and Shore 00-50 has the lowest hardness, 00-50. In our experiments, both 10F and 20M are mixed with 20% mineral oil by weight to reduce stiffness and friction during insertion. The 10M and 00-50 are mixed with 10% mineral oil by weight. The Tensile Strength is between 315psi to 550psi, with shrinkage less than 0.001 inches.[24,25] To estimate Young's modulus of tissues, durometer scale A and durometer scale 00 were developed by Larson et al.[26,27] In our experiments, Young's modulus of shore 00-50 can be estimated as:

$$E = (0.0037)e^{(0.0718)S} \tag{1}$$

where E is Young's modulus in MPa and S is nominal Shore 00 durometer hardness;
Young's modulus of shore 10 Fast, Shore 10 Medium and Shore 20 Medium can be estimated as:

$$E = (0.4863)e^{(0.0345)S} \tag{2}$$

where E is Young's modulus in MPa and S is nominal Shore A durometer hardness. Both Young's modulus and the Shore hardness of tissue phantoms are shown in the Table 1.

Table 1: Young's modulus and Shore hardness of tissue phantoms

Tissue	**Approximate Young's modulus(kPa)**	**Shore hardness**
15%SEBS	68.0	
20%SEBS	128.0	
00-50	134.0	00-50
10 Fast	687.0	10A
10 Medium	687.0	10A
20 Medium	970.0	20A

Poly (styrene-b-ethylene-co-butylene-b-styrene) triblock copolymer (SEBS) produced by Kraton Polymers LLC (G1652, Houston, TX, USA) is used as the base material for the second group of tissues used in our experiments. The density of this material is $\rho_{SEBS} = 910\frac{kg}{m^3}$. Mineral oil is used as the solvent for this material. According to R.A. Mrozek *et al.*,[28] the stiffness of the tissue is not dependent on the supplier of the mineral oil. The authors used light mineral oil with density $\rho_{oil} = 0.85\frac{g}{mL}$.

SEBS material and mineral oil are weighed out to produce mixtures containing 15, and 20vol% SEBS. The mixture was then put into the oven at 120^oC for 8 hours (for mixtures containing lower amount of SEBS this time is lower) and was mixed occasionally to produce a homogeneous solution without any visible undissolved powder. The solution is then poured into mold of rectangular shape with dimensions $100 \times 100 \times 50\,mm$ and let to cool down in room temperature before removing from the mold. In order for the tissue to come off easily, universal mold remover was used.

From the log-log plot of Young's modulus vs. polymer fraction provided in R.A. Mrozek *et al.*[28] we found that there is a power law relationship between the Young's modulus and the polymer fraction as follows:

$$\text{Young's modulus} = c(\text{Polymer fraction})^m \tag{3}$$

With $m = 2.2234$ and $c = 4.6018 \times 10^6$. In this equation, the polymer fraction is in percents and the Young's modulus is calculated in Pascals (Pa). Therefore, the elastic moduli for 15% and 20% SEBS are $\approx 68kPa$ and $128kPa$, respectively that are also relevant to stiffness of biological tissues within human body.[29] These values are consistent with the values reported in the paper and that the power law can be extended to find the Young's modulus of tissues with SEBS concentration less than 20%. It's also worth mentioning that the authors examined samples of cylindrical soft gels with diameter of $25\,mm$ and thickness of $2\,mm$ using a rheometer to verify the results presented in R.A. Mrozek *et al.*[28] Rheological tests are done at 25^oC (because in a region with center at 20^oC, the modulus shows less sensitivity to temperature[28] and needle insertion experiments are usually performed in room temprature) with $1Hz$ frequency and strain range is within $0.01\% \sim 5\%$ to ensure linear viscoelastic response of these gels. The shear modulus obtained from rheometer is converted to Young's modulus (E) considering Poisson's ratio of $\nu \approx 0.5$ for an incompressible solid and using the equation $E = 2G(1 + \nu)$ where G is the shear modulus obtained from rheology experiments.

2.2. *Recoverable Strain and Nitinol Stylet Heat Treatment*

The stylets used in the experiment were made of superelastic nitiol. As such, computing the maximum recoverable strain is a necessary condition when determining the minimum radius of stylet curvature. To ensure that the stylet can be fully straightened without any plastic deformation, we decide to use the common conservative superelastic Nitinol strain limit of $\varepsilon = 8\%$.[22] The relationship between recoverable strain limit and needle tip pre-curvature is:

$$\kappa = \frac{2\epsilon}{D(1+\epsilon)} \tag{4}$$

Then the calculated minimum radius of needle curve, r, is derived from

$$\kappa = 1/r. \tag{5}$$

For the needle used in our experiments described in Table 2 and Table 3, the minimum radius of 0.47mm diameter stylet without plastic deformation is 3.1718mm, and the minimum radius of 0.25mm diameter stylet without plastic deformation is 1.7145mm.

Table 2: Parameters of tube and needle for silicone compound tissue phantoms

parameters	**tube**	**needle**
outer diameter(mm)	0.8	0.47
inner diameter(mm)	0.6	–
length(mm)	350	400

Table 3: Parameters of tube and needle for SEBS tissue phantoms

parameters	**tube**	**needle**
outer diameter(mm)	1.45	0.25
inner diameter(mm)	0.7	–
length(mm)	200	220

To achieve a balanced bending stiffness relationship among tissue, stylet and tissue phantom, the tube in Table 3 was 3D printed with SemiFlex, a material with 25Mpa Young's Modulus that dropped 3 folds in comparison to the Young's Modulus of the Nitinol tube, 40Gpa.

To fabricate the optimal shape for each Nitinol stylet geometry, straight Nitinol pieces are pressed in an aluminum mold, heated to $500°C$ for 30 minutes, then quenched with water. Figure 2 shows the three stylet geometries after heat treatment that are used during experimentation.

Fig. 2: Three different needle shapes (A) Arc-stylet (B) Spiral-stylet (C) Right Angle-stylet

2.3. *Experimental device setup*

To achieve high steerability inside tissues, there are three separate motions needed. First, the stylet with predefined geometry and the tube that encases the stylet must be able to be moved relative to each other. Second, the stylet and tube need to be rotated simultaneously. Through these two motions, steerability in 6 degrees of freedom can be achieved. To accomplish this, the main part of the needle insertion system consists of two linear slides and one rotational servo motor. Other components, including limit switches, collets and bearings, are connected to the main structure by 3D printed parts and traditional fasteners. The linear slide and servo motor are controlled by microstep drivers to achieve accurate linear motion and the rotational servo achieves accurate rotational motion through internal feedback. The control of the needle insertion device is accomplished through firmware running on a chipKit uC32 microcontroller (Digilent Inc., Pullman, WA, USA), which accepts simple linear and rotational velocity commands from a PC running control scripts in the Python environment. The microcontroller is continually monitoring the status of the limit switches to ensure no portion of the system is driven past its physical limits.

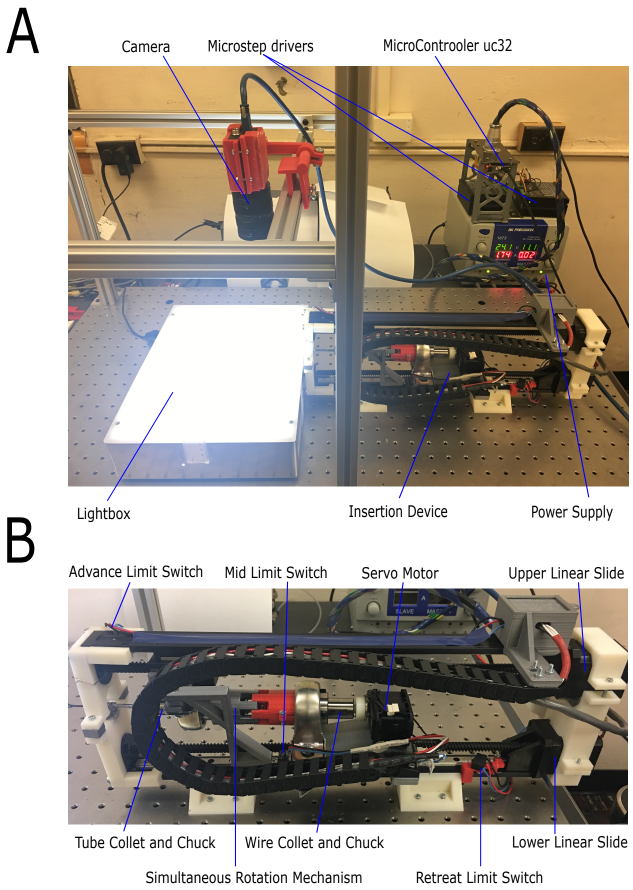

Fig. 3: (A) The whole needle insertion system setup, including the insertion device, two micro step drives for linear slides, a light box, a camera, a microcontroller, and a power supply.(B) Insertion device setup, including three limit switches, simultaneous rotation mechanism, tube and wire collets and chucks, two linear slides and two bearings.

Figure 3-A shows the overall system with the insertion device, overhead camera capture, a lightbox for transparent tissue simulant , and the associated electronics. Figure 3-B depicts the assembly of the insertion system, with each critical component labeled. Each collet and bearing was mounted on the opposing linear slides, such that the bores of the collets are collinear. The tube collet is located distally, closest to the insertion point, and the wire collet is located proximally, such that the wire can be pushed out of the tube. Three limit switches are located at the most distal limit of travel, the most proximal limit of travel, and between the wire and tube stages.
A typical insertion consists of the following steps:

(1) The wire platform moves backward until retreat limit switch activated. The tube collet follows needle platform to move back until inter-stage limit switch activated.
(2) Send a step length for moving forward motion, the wire collet moves first, then the tube platform follows it.
(3) Send a rotation angle, if necessary, to the servo motor to rotate the tube and wire.
(4) Repeat Step 2 and Step 3 until the needle tip reaches the desired position.

3. Results

This section describes the experimental results obtained from multiple sets of experiments done using different needle shapes, different tubes and different tissue phantoms. Ten experiments for each step length are performed and the average of the experiments are obtained to reduce the error. This section is categorized in three subsections. In the first subsection, we demonstrated how to control the direction of insertion with rotation of needle. Subsection 2 presents controlling the insertion curvature with different step lengths. At the end, the third subsection demonstrates that there exists a linear relationship between insertion curvature and step length.

3.1. *Insertion Direction*

In these series of experiments, we showed how to control insertion direction. As can be seen from the Figure 4 and Figure 5, the direction of insertion can be reoriented by the rotation of the wire collet. Figure 4 depicts the first advancement of the inner stylet in the opposite direction from the initial curvature in the silicone compound tissue. As shown, both needle and tube originally exhibit a clockwise curvature; however, after the stylet and tube were rotated 180 degrees, the curvature is now directed in the counter-clockwise direction. When rotating, the stylet has to be retracted back into the tube first. Figure 5 represents a triple-bend tube following the stylet each step after reorientation inside SEBS tissue.

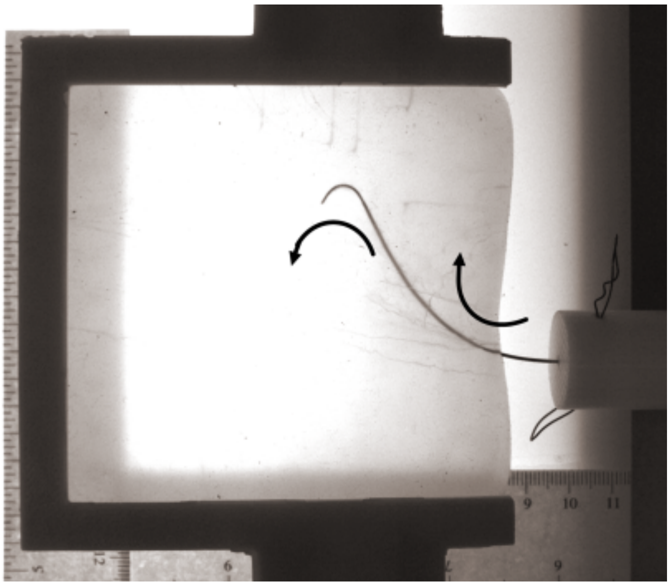

Fig. 4: Rotation of the stylet changes direction of subsequent stylet insertions into silicone compound tissue.

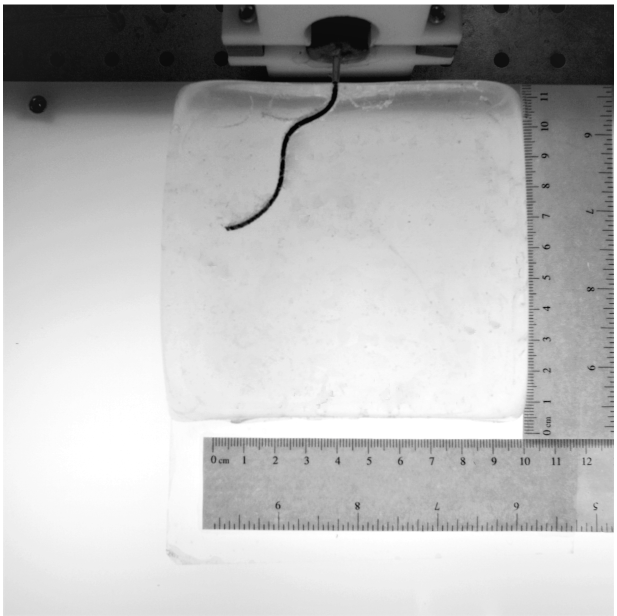

Fig. 5: Triple bends after re-orientation of the stylet and subsequent steps with SemiFlex tube in SEBS tissue phantom.

3.2. *Insertion Curvature*

The technique we have used for needle path tracking is based on image analysis. By fitting a curve on top view of insertion image, the insertion curvature of each needle can be obtained. As shown in Figure 6, as the step length increases, the wire comes out of the tube corresponding to further distance per step, which causes the needle arc length to rise. In the case of the spiral stylet, this corresponds to a changing curvature, but in the cast of the arc and right angle stylets, a constant curvature. The needle showed in Figure 6 is the Arc-stylet shape.

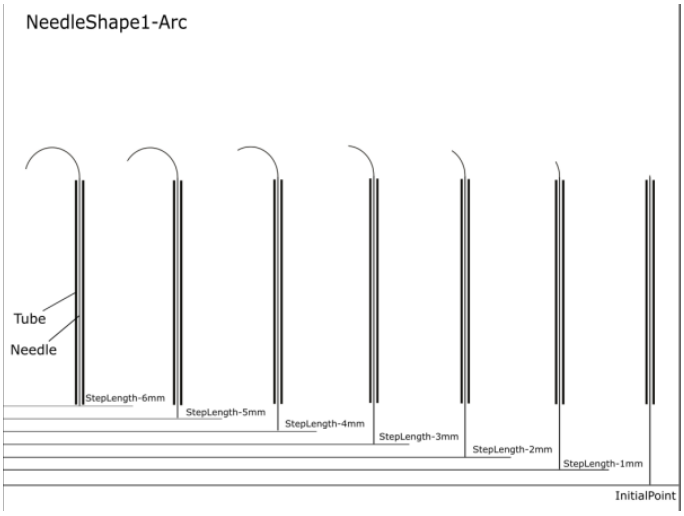

Fig. 6: Depiction of how the stylet step length causes a longer channel to be cut in the tissue.

In a single insertion, there are three different states of curvature, as shown in Figure 1:

(1) Initial state: Before the insertion, the relatively low tube stiffness is not enough to straighten pre-curved wire completely. Some amount of curvature is evident when tube and wire are fully overlapped.
(2) Stylet insertion: The stylet goes into tissue, cutting a channel based on its preset curvature.
(3) Tube follows stylet: The stiffness of tissue is insufficient to make the tube follow the exact path of the stylet, so the resultant shape is based on the stored elastic energy of the stylet, tube, and tissue. In our experiments where the tube stiffness is of the same order of magnitude as the tissue, the actual insertion curvature is less than stylet curvature.

Figure 7 demonstrates the insertion curvatures of different step lengths inside the tissue phantom. The needle type used here is Arc-Stylet shape.

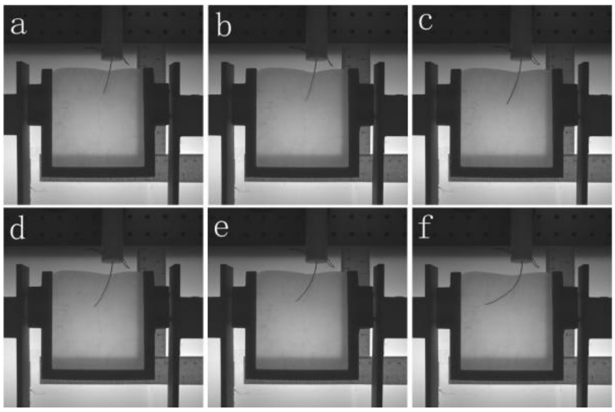

Fig. 7: Changing the step length in the same tissue sample changes the curvature accordingly.

3.3. *Curvature as a Function of Step Length*

Though the radius decreases with decreased step length, a characterization of the relationship between radius, step length, stylet geometry, and tissue stiffness is necessary. For each combination of tissues and stylet shapes, we have used several equal-interval step lengths to get different curvatures of needle insertion. Figure 8 demonstrates the relationship between the achievable radius with step length for different silicon compound tissue phantoms. This figure depicts the relatively linear relationship between the radius and step length for four different tissue phantoms with three different stylet shapes. Ten experiments are done for each step length and the average of data is obtained to reduce error. The error bars shown are standard deviation from the mean. For the heat treatment, Nitinol tube was heated up to 500^oC then let to be at 450^oC for 30 minutes, and then let to cool down to room temperature in the oven. The tissue phantom used in Figure 8D, 00-50, has the lowest Young's Modulus of 134 kPa among silicone compound tissues. In this tissue phantom, a slight lateral motion can be observed when the tube follows an inserted needle with long step length. The cause of this lateral motion is the unbalanced bending stiffness relationship among tissue, stylet and tube.

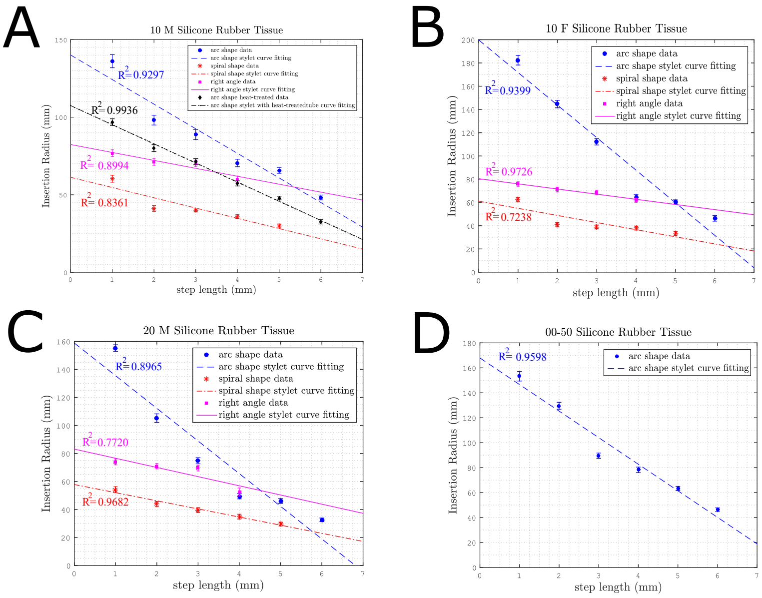

Fig. 8: Radius as a function of step length in different silicone compound tissue phantoms. The bars on the data points are Standard Deviation of the data. Ten experiments are done for each step length and the average of the data are calculated to minimize error. The curve fitting and R-squared value indicates the relatively linear relationship between the step length and the radius. Young's Modulus of each tissue can be found at Table 1. (A) Curvature as a function of step length in 10M tissue phantom. The heat-treated Arc-shape stylet has lower radius than non-heat-treated one because of the decrease in bending stiffness caused by heat treatment. (B) Relationship between radius and step length in 10F tissue phantom. (C) Curvature as a function of step length in 20M tissue phantom. (D) Curvature as a function of step length in 00-50 tissue phantom

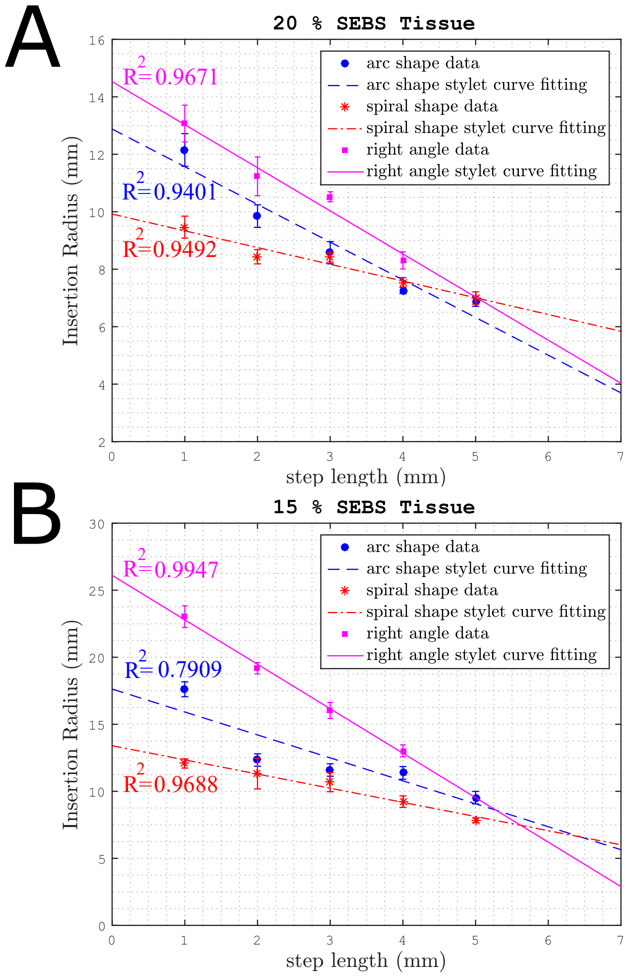

Fig. 9: Curvature as a function of step length in two different SEBS tissue phantoms. The error bars show the standard deviation. The curve fitting and R-squared value indicate the relatively linear relationship between step length and curvature. The tube and stylet used with SEBS tissues are different from previous type used with silicone compound tissue. The parameters of stylets and tubes can be found in Table 2 and Table 3. (A) Curvature as a function of step length in 20% SEBS tissue phantom. (B) Curvature as a function of step length in 15% SEBS tissue phantom.

3.4. *Insertion Radius and The Relationships among Tissue Bending Stiffness, Tube Bending Stiffness and Wire Bending Stiffness*

The resultant insertion radius of the proposed stepping stylet and tube method is wholly dependent on the relationship between the bending stiffness of the tissue, K_t, the bending stiffness of the tube, K_b, and the bending stiffness of the wire, K_w. A very course description of an appropriate relationship of K_t, K_b and K_w is that $K_t > K_b > K_w$. Where the stylet geometry is often very small and stores very little elastic energy in bending, the most essential relationship is $K_t > K_b$. This relationship is derived from experimental data presented in this paper using and the equations relating the bending stiffness and curvatures of mutliple overlapping curved tubes by Webster *et. al.*:[22]

$$\kappa_C = \frac{\sum_{i=1}^{n} E_i I_i \kappa_i}{\sum_{i=1}^{n} E_i I_i} = \frac{K_t\kappa_t + K_b\kappa_b + K_w\kappa_w}{K_t + K_b + K_w} \tag{6}$$

where κ_C is the combined curvature after the tube is fully overlapping the wire inside the tissue channel, and κ_t, κ_b, κ_w and K_t, K_b, K_w are the curvature and bending stiffness of the tissue channel, tube, and wire, respectively. I_i is the cross-sectional moment of inertia and E is the Modulus of Elasticity(Young's Modulus).

$$K_i = E_i I_i \tag{7}$$

The product of the Modulus of Elasticity and cross-sectional moment of inertia is bending stiffness. Here we are making a simplifying assumption and treating the channel that has been cut in the tissue as an outer tube. Because of the relatively small strains of the tissue using the relative stiffness heuristic, this simplifying assumption is valid.

If the tube bending stiffness is slightly higher than the tissue bending stiffness, it will cause an observable increase of the insertion radius. If the the tube bending stiffness is significantly higher than the tissue bending stiffness, a significant straightening of the tissue channel will be observed and the tissue will undergo large strains.

Figure.9 shows the experimental results obtained by changing tube material from Nitinol to SemiFlex to satisfy the bending stiffness relationship between tube and tissue phantom. Furthermore, to adjust the stylet bending stiffness to match the tube, we picked a Nitinol stylet with smaller diameter. The tissue phantoms used are 15% and 20% concentration SEBS. Comparing the silicone results shows in Figure 8 with those for the much more compliant tissues shown in Figure 9, the drastic improvement in the radius of curvature is due directly to the higher tissue stiffness relative to the tube and wire stiffness. Additionally, Figure 9A and Figure 9B show that when the tissue stiffness is decreased while using the same tube and wire stylet, the insertion radii of all three kind of stylet shapes are increased. The two factors that will cause the change of tube bending stiffness, given a fixed material Young's modulus, are tube diameter and tube wall thickness.

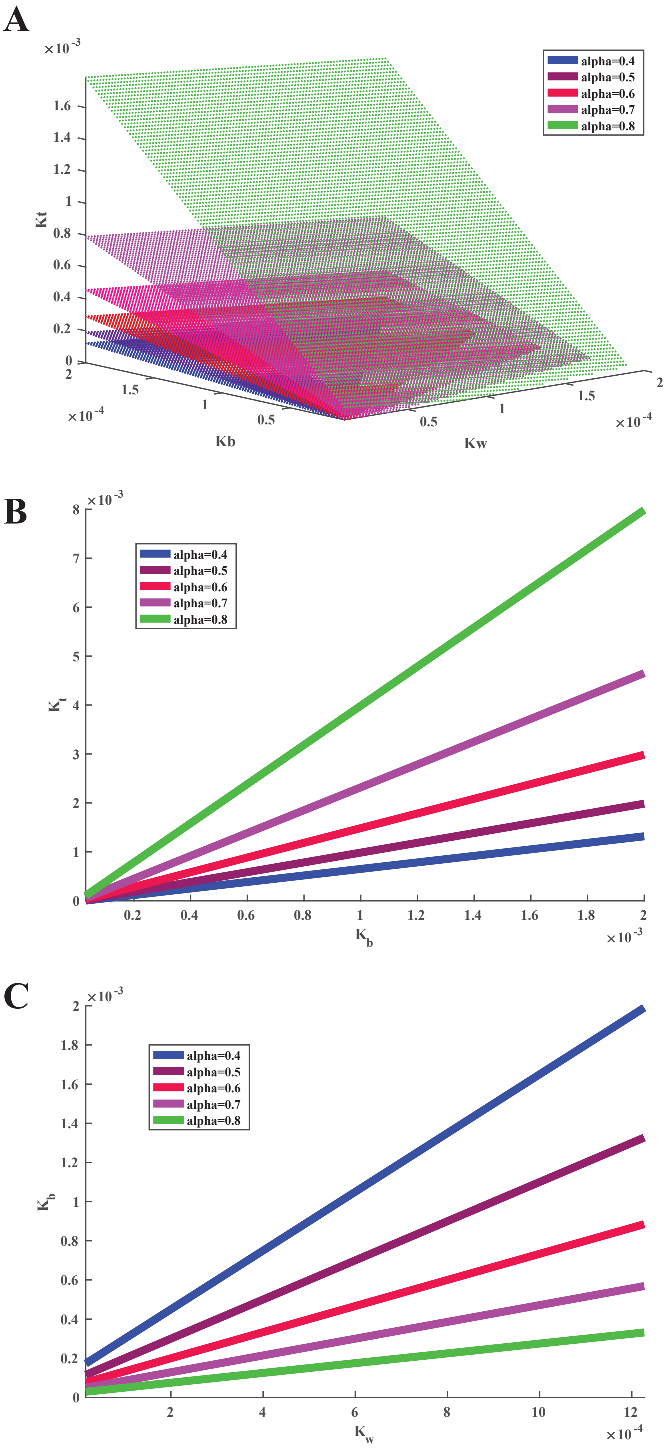

Fig. 10: A simplified relationship between the curvature of the overlapped wire, tube, and tissue as a function of the bending stiffnesses of each of these components. The simplifications to the general relationship given in Equation (6) is that we assume the curvature of the tube is zero, $\kappa_b = 0$, the curvature of the tissue channel and the wire are equivalent, $\kappa_t = \kappa_w$, and we examine the specific cases where the curvature of the combined wire, tube, and tissue is a constant fraction of the curvature of just the wire stylet ($\kappa_C = \alpha\kappa_w$, where $0 < \alpha < 1$). (A) A plot of the simplified relationship between the stiffnesses for five different curvature ratios. The general trend is that as the tube and wire stiffness increases the tissue stiffness must also increase to maintain the same curvature ratio. (B) For a fixed tissue channel bending stiffness, K_t, the relationship between wire and tube stiffnesses that maintains the curvature of the overlapping configuration. (C) For a fixed wire bending stiffnes (i.e. a particular wire diameter and material), the relationship between the tube bending stiffness (i.e. a particular tube diameter, wall thickness, and material) and the tissue bending stiffness that maintains the curvature of the overlapping configuration.

Figure.10 shows a simplified tissue, wire and tube relationship for a single step length. We assume the curvature of the tube is zero, and the curvature of the tissue channel is equivalent to the wire. These simplifying assumptions turn Equation (6) into the simplified form:

$$0 = (1-\alpha)K_w K_t - \alpha K_b + (1-\alpha)K_w \qquad (8)$$

Equation (8) describes a planar surface in K_w, K_t, and K_b. Note that the relationship no longer depends on curvature terms, such that the stiffness relationships between tissue, tube, and wire hold true for any curvature of the wire and the tissue channel it cuts.

The proper establishment of relationships among K_t, K_b and K_w will bring a high steerability to the system. By selecting wires and tubes that have much lower bending stiffness than the tissue, the insertion radius have the tendency to be reduced to the nearly the curvature of the pre-shaped wire stylet.

3.5. *Modeling of Pre-curved needle*

The bicycle model is the most common model used to describe the motion of bevel-tipped and pre-bent steerable needles.[5, 6, 30] It generally prescribes the motion of the steerable needle in terms of a fixed rate of angular rotation in a plane as a function of insertion velocity and the ability to re-orient the plane in which the needle is traveling by twisting the needle at the base.

Here, we present a discrete analogue of the bicycle model for the proposed method of fracture-directed needles. In this model, the independent variable is now the step length of the stylet before following with the tube.

Consider a pre-curved stylet that is driven by step length from the end of the tube. As the stylet exits the tube and enters the tissue, the stylet will nominally follow the predefined shape of the stylet. The step length is modeled as the input to the system. In the following subsection, mathematical preliminaries to propose a suitable model will be investigated. Then, a model based on Lie groups and Lie algebra will be proposed and finally the simulation results indicating the relationship between the curvature and step length will be given. The model for the curvature as a function of step length is derived from the experimental results presented in Figure 8. In this section a mathematical model is developed for position of needle tip with respect to the base frame as a function of the step lengths. Figure 11 shows the three distinct stages of needle insertion into the tissue.

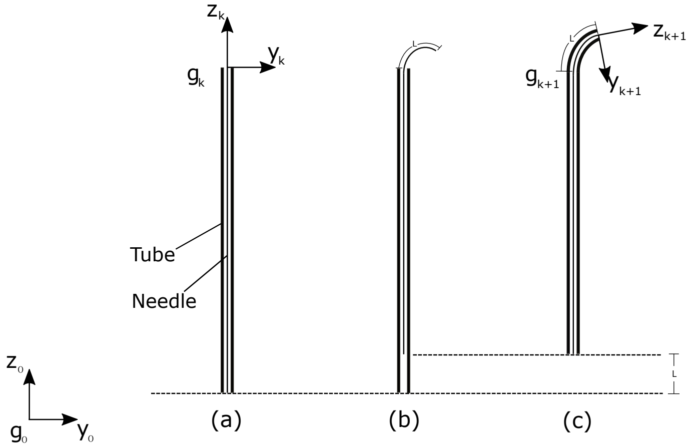

Fig. 11: position and orientation of needle tip

First, the stylet is extended out of the tube, after which the tube follows the stylet. The z-axis of the body fixed frame is the direction of insertion. The arc length of each step is parameterized by l, in millimeters.

In order to find the position and orientation of needle with respect to the base frame, a model is developed for the relationship between the curvature, κ, the step length, l, and the rigid body motion between the body fixed frames, g_k and g_{k+1}, before and after the completed step, as shown in Figure 11(a),(c). The twist coordinates of the system are defined as follows:

$$\xi(l) = \begin{bmatrix} \omega \\ v \end{bmatrix} = \begin{bmatrix} \kappa(l) \\ 0 \\ 0 \\ 0 \\ 0 \\ 1 \end{bmatrix} \tag{9}$$

The twist describes the discrete-step needle motion and is a function of l, which is the length of the needle that is inserted before the tube follows.

By inspection of the vector field defined by the twist, the needle system has rotation around the body-fixed x-axis and linear translation along the z-axis. Using the matrix exponential of the twist describing the motion in each discrete step of the stylet and tube, the pose of the needle after a step can be calculated as the product of matrix exponential of the twist and the previous pose,

$$g_{k+1} = e^{\hat{\xi}_k l} g_k. \tag{10}$$

The discrete-step position/ orientation change is only a function of the length of the needle that is inserted before the tube follows. The matrix $g_k \in SE(3)$ is the tube tip position/orientation before the needle is inserted and $g_{k+1} \in SE(3)$ is the tube tip position/orientation after the needle has been inserted and the tube has followed. This model can be used, based on experimentally determined curvature as a function of step length, $\kappa(l)$, to simulate needle insertions for any number of steps and for any step length along the way. In this section, simulation results demonstrating the change of needle insertion radius are investigated. With this simulation, the insertion radius with long step length can be predicted disregard the restriction of tissue phantom szie. Use arc shape stylet in Shore 10M tissue simulant as an example, the values of radius for different values of step lengths are shown in Table 4.

Table 4: Arc-stylet insertion radius for different values of step lengths

step length(mm)	**radius(mm)**
1	136.09
2	98.13
3	88.79
4	70.48
5	65.70
6	48.25

Curve fitting using MATLAB (The MathWorks, Inc., Natick, Massachusetts, United States) showed that the relationship between radius and step length can be approximated by a line with the following equation

$$\kappa = 0.002l + 0.0057 \tag{11}$$

Figure 12 depicts the radius change as a linear function of needle insertion radius for different step lengths. This linear relationship between the insertion radius and the step length allows precise prediction of the insertion radius across insertions with larger step lengths.

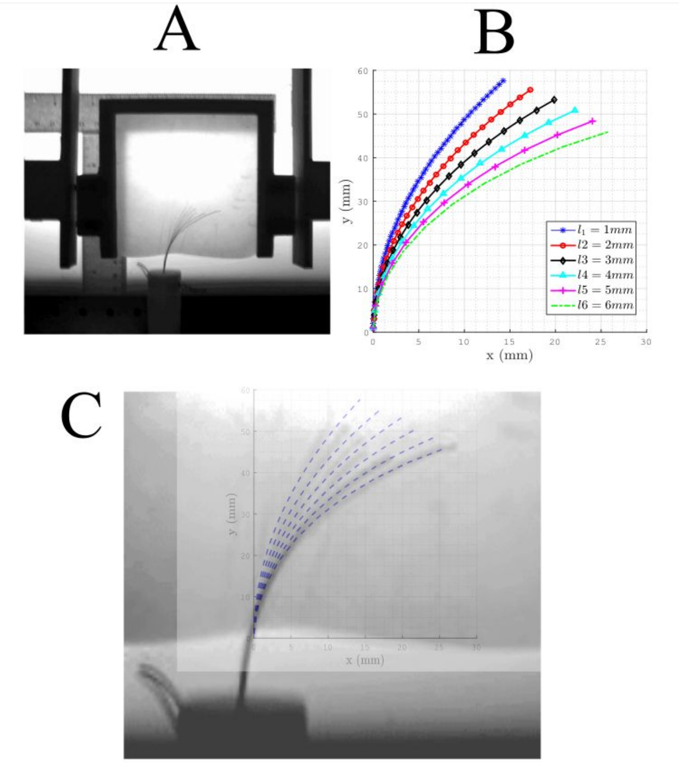

Fig. 12: (A) An overlay of multiple real trials with differing step lengths, demonstrating the curvature increase as the step length increases. (B) The model based on real experiments, provide the capability of predicting insertion radius with large step lengths. (C) An overlay of experimental insertion radii (black continuous curves) and model generating insertion radii (blue dashed curves), which shows the reliability of the model.

4. Discussion

4.1. *Similar Insertion Radius across a Range of Young's Modulus of The Tissue Phantoms*

Experimental data of various stylet shapes, tube materials and different tissue phantoms demonstrates that once an appropriate bending stiffness relationship among tissue phantoms, stylets, and tubes is established, an approximately linear relationship between insertion radius and step length can be achieved. Figure 8 shows that this fracture-directed method of steering results in a small change in the radius across a certain range of Young's modulus of the tissue phantoms. Figure 9 shows that a doubling in the Young's modulus between the 15% and 20% SEBS tissues resulted in 20-40% change in the insertion radius. This is an observable increase of insertion radius, but the modeling presented provides a method of determining an upper bound on the curvature for the most compliant tissue that will be encountered in an insertion and feedback control can achieve any curvature lower that the maximum through the step length control. Figure 10 B explained the phenomenon appeared in SEBS tissue phantom and demonstrates the tissue agnostic behavior. As the bending stiffness of the tube and stylet become low compared to the tissue bending stiffness (the situation in SEBS tissue), the tissue bending stiffness can vary by a large amount while having a small effect on the effective resultant combined curvature. Once the bending stiffness of the tube and stylet become high compared to the tissue bending stiffness (situation in silicon tissue), any softer tissue will result in a rapid degradation of the achievable insertion curvature. Thus the objective should be to create stylets and tubes with as low of bending stiffness as possible while still maintaining the ability to effectuate cutting.

Additionally, the lowest insertion radius attained in experiments with silicone compound tissue phantom using Nitinol tube is 29.58mm, and the lowest insertion radius attained in experiments with SEBS tissue phantom using SemiFlex tube is 6.88mm. To the authors' knowledge, this is the best reported radius of curvature achieved among all needle steering methods.

4.2. *Insertion Radius is linear as a function of step length*

The achievable insertion radius, as a function of the step length of the stylet out of the tube before following with the tube, can be fit with a high degree of accuracy to a line. The curve fitting and the goodness of fit are shown in Figure 8 and Figure 9. For each of the stylet designs, those two figures also demonstrates that the linear relationship between step length and curvature is only valid for a limited range of the insert lengths tested. While having a linear relationship is not necessary for accurate control, it does simplify the process of simulation and control. For the right angle stylet, the curved region of the stylet has fully exited the tube at the $4mm$ step length, thus any additional insertion becomes less effective and the linear fit is only computed using the $1mm$ through $4mm$ step lengths.

4.3. *Insertion Radius Variability*

Another observation from the data is that generally, the standard deviation of the insertion radius decreases as the step length increases. There is a reasonable explanation for the possibility of this variability decrease. In the stylet insertion stage, when the needle is attempting to begin to fracture the tissue phantom, it first deforms the tissue until the fracture begins. With small step lengths, it is possible that some of the steps only deform the tissue and do not cause a fracture to begin. As such, the failure to fracture the tissue, or to have a larger deformation and smaller fracture distance, would result in a deviations from a scenario where the fracture and stylet step were perfectly coincident. A similar behavior occurs in tube-follow stage when the tube is trying to follow the path created by the stylet.

Additionally, some of the variability in the insertion radius occurs because of the inexact angle in which the needle initially punctures the tissue. For larger stylet step lengths, the initial steps penetrate further into the tissues and create a better tissue anchor near the surface. Consequently, as the step length increases, the relationship between curvature and step length will be more stable.

There are two immediate solution to minimize variability due to the deformation of tissue phantom. The first is to reduce the bending stiffness of the tube. Although the tube bending stiffness satisfies the appropriate relationship, the tubes used in experiments still have a relatively high bending stiffness. As such, when the tube follows the stylet, it is deforming the tissue more than it is necessary. Seeking a soft or thin tube that has much lower bending stiffness than the tissue phantom will help to decrease the insertion radius and also improve the stability of it. So, a primary focus of future work will be on the identification and modeling of the interaction between tissues, tubes, and stylets of different stiffnesses to optimize the needle and stylet selection for extremely soft biological tissues. The secondary objective will be the fabrication of stylet tips that are able to fracture the tissue more easily.

5. Conclusion

We have presented the design, assembly, proposed control, and analysis of a new class of needle insertion system, which we have called fracture-directed steerable needles. This system currently has the capability to control the insertion in two-dimensional space by changing the servo motor rotation angle and the step length of the stylet relative to the tube which will follow. A comprehensive analysis based on material stiffness, single insertion step length and insertion radius were given. This analysis provided a functional model about the radius-step length relationship for three different stylet geometries and across three tissue simulants with more than an order of magnitude variability in Young's Modulus. A linear relationship between the radius and stylet step lengths for each tissue stiffness was also established.

We have additionally presented a preliminary bending moment analysis between the tube, tissue, and needle. By selecting the wire stylet and tube geometries based on the bending stiffness of the channel cut in the tissue, approximated as an outermost tube, the proposed method is capable of achieving high curvature across all tissue having higher stiffness than the tissue for which the tube and wire were selected.

The immediate future work is the application of fracture-directed steerable needles to the three-dimensional space and building a predictive model based on Young's modulus of tissue, stylet, and tube, geometry of the stylet, and step lengths that allow us to model the interaction in real tissue samples. This closed-loop control of the curvature will provide the ability to actively control to any planned path above the minimum radius of curvature of the wire, tube, and tissue combination. For steerable needles, there are wide clinical and industrial applications for which the proposed work provides a new class of needles for future research.

References

[1] P. J. Swaney, A. W. Mahoney, B. I. Hartley, A. A. Remirez, E. Lamers, R. H. Feins, R. Alterovitz and R. J. Webster III, Toward transoral peripheral lung access: Combining continuum robots and steerable needles, *Journal of Medical Robotics Research* (2016) p. 1750001.

[2] M. Abayazid, P. Moreira, N. Shahriari, A. Zompas and S. Misra, Three-dimensional needle steering using automated breast volume scanner (abvs), *Journal of Medical Robotics Research* **1**(01) (2016) p. 1640005.

[3] P. Moreira, G. van de Steeg, T. Krabben, J. Zandman, E. E. Hekman, F. van der Heijden, R. Borra and S. Misra, The miriam robot: A novel robotic system for mr-guided needle insertion in the prostate, *Journal of Medical Robotics Research* (2016) p. 1750006.

[4] N. J. Cowan, K. Goldberg, G. S. Chirikjian, G. Fichtinger, R. Alterovitz, K. B. Reed, V. Kallem, W. Park, S. Misra and A. M. Okamura, Robotic needle steering: Design, modeling, planning, and image guidance, *Surgical robotics*, (Springer, 2011), pp. 557–582.

[5] R. J. Webster III, J. S. Kim, N. J. Cowan, G. S. Chirikjian and A. M. Okamura, Nonholonomic modeling of needle steering, *Int. J. Robot. Res.* **25** (May 2006) 509–526.

[6] W. Park, J. S. Kim, Y. Zhou, N. J. Cowan, A. M. Okamura and G. S. Chirikjian, Diffusion-based motion planning for a nonholonomic flexible needle model, *Proc. IEEE Int. Conf. Robot. Autom.*, IEEE, Barcelona, Spain (April 2005), pp. 4600–4605.

[7] N. J. van de Berg, T. L. de Jong, D. J. van Gerwen, J. Dankelman and J. J. van den Dobbelsteen, The influence of tip shape on bending force during needle insertion, *Scientific Reports* **7** (2017) p. 40477.

[8] T. K. Adebar, J. D. Greer, P. F. Laeseke, G. L. Hwang and A. M. Okamura, Methods for improving the curvature of steerable needles in biological tissue, *IEEE Transactions on Biomedical Engineering* **63**(6) (2016) 1167–1177.

[9] M. Scali, T. P. Pusch, P. Breedveld and D. Dodou, Needle-like instruments for steering through solid organs: A review of the scientific and patent literature, *Proceedings of the Institution of Mechanical Engineers, Part H: Journal of Engineering in Medicine* (2016) p. 0954411916672149.

[10] W. Park, K. B. Reed, A. M. Okamura and G. S. Chirikjian, Estimation of model parameters for steerable needles, *Proc. IEEE Int. Conf. Robot. Autom.*

(may. 2010) 3703 –3708.

[11] J. A. Engh, D. S. Minhas, D. Kondziolka and C. N. Riviere, Percutaneous intracerebral navigation by duty-cycled spinning of flexible bevel-tipped needles, *Neurosurgery* **67**(4) (2010) 1117–1123.

[12] G. Gerboni, J. D. Greer, P. F. Laeseke, G. L. Hwang and A. M. Okamura, Highly articulated robotic needle achieves distributed ablation of liver tissue, *IEEE Robotics and Automation Letters* (2017).

[13] A. J. Petruska, F. Ruetz, A. Hong, L. Regli, O. Sürücü, A. Zemmar and B. J. Nelson, Magnetic needle guidance for neurosurgery: Initial design and proof of concept, *Robotics and Automation (ICRA), 2016 IEEE International Conference on*, IEEE (2016), pp. 4392–4397.

[14] K. B. Reed, A. M. Okamura and N. J. Cowan, Modeling and control of needles with torsional friction, *IEEE Trans. Biomed. Eng.* **56** (December 2009) 2905–2916, NIHMS192959.

[15] J. P. Swensen and N. J. Cowan, Torsional dynamics compensation enhances robotic control of tip-steerable needles, *Robotics and Automation (ICRA), 2012 IEEE International Conference on*, IEEE (2012), pp. 1601–1606.

[16] M. Khadem, C. Rossa, N. Usmani, R. S. Sloboda and M. Tavakoli, Introducing notched flexible needles with increased deflection curvature in soft tissue, *Advanced Intelligent Mechatronics (AIM), 2016 IEEE International Conference on*, IEEE (2016), pp. 1186–1191.

[17] V. K. Bui, S. Park, J.-O. Park and S. Y. Ko, A novel curvature-controllable steerable needle for percutaneous intervention, *Proceedings of the Institution of Mechanical Engineers, Part H: Journal of Engineering in Medicine* **230**(8) (2016) 727–738.

[18] P. J. Swaney, J. Burgner, H. B. Gilbert and R. J. Webster, A flexure-based steerable needle: high curvature with reduced tissue damage, *IEEE Transactions on Biomedical Engineering* **60**(4) (2013) 906–909.

[19] H. B. Gilbert, J. Neimat and R. J. Webster, Concentric tube robots as steerable needles: Achieving follow-the-leader deployment, *IEEE Transactions on Robotics* **31**(2) (2015) 246–258.

[20] M. Neumann and J. Burgner-Kahrs, Considerations for follow-the-leader motion of extensible tendon-driven continuum robots, *Robotics and Automation (ICRA), 2016 IEEE International Conference on*, IEEE (2016), pp. 917–923.

[21] S. Okazawa, R. Ebrahimi, J. Chuang, S. E. Salcudean and R. Rohling, Hand-held steerable needle device, *IEEE/ASME Transactions on Mechatronics* **10**(3) (2005) 285–296.

[22] R. J. Webster III, J. M. Romano and N. J. Cowan, Mechanics of precurved-tube continuum robots, *IEEE Transactions on Robotics* **25**(1) (2009) 67–78.

[23] P. E. Dupont, J. Lock, B. Itkowitz and E. Butler, Design and control of concentric-tube robots, *IEEE Transactions on Robotics* **26**(2) (2010) 209–225.

[24] I. Smooth-On, Addition cure silicone rubber compounds product and technical review @MISC (May 2017).

[25] I. Smooth-On, Super-soft, addition cure silicone rubbers product and technical review @MISC (May 2017).

[26] J. D. Pampush, D. J. Daegling, A. E. Vick, W. S. McGraw, R. M. Covey and A. J. Rapoff, Technical note: Converting durometer data into elastic modulus in biological materials, *American journal of physical anthropology* **146**(4) (2011) 650–653.

[27] H. Qi, K. Joyce and M. Boyce, Durometer hardness and the stress-strain behavior of elastomeric materials, *Rubber chemistry and technology* **76**(2) (2003) 419–435.

[28] R. A. Mrozek, B. Leighliter, C. S. Gold, I. R. Beringer, H. Y. Jian, M. R. VanLandingham, P. Moy, M. H. Foster and J. L. Lenhart, The relationship between mechanical properties and ballistic penetration depth in a viscoelastic gel, *Journal of the mechanical behavior of biomedical materials* **44** (2015) 109–120.

[29] P. N. Wells and H.-D. Liang, Medical ultrasound: imaging of soft tissue strain and elasticity, *Journal of the Royal Society Interface* **8**(64) (2011) 1521–1549.

[30] T. R. Wedlick and A. M. Okamura, Characterization of pre-curved needles for steering in tissue, *Engineering in Medicine and Biology Society, 2009. EMBC 2009. Annual International Conference of the IEEE*, IEEE (2009), pp. 1200–1203.

Fan Yang received his B.S. in Mechanical Engineering from the Shanghai Institute of Technology. He is currently pursuing his Ph.D. degree in the Department of Mechanical Engineering at Washington State University. He is a graduate research assistant in the Modeling, Motion, and Medical (M3) Robotics Laboratory under the supervision of Dr. John P. Swensen. His research interests include steerable needles, continuum robotics, and medical devices.

Mahdieh Babaiasl received her M.S. degree in Mechatronics from the University of Tabriz, Iran. From 2011 to 2013, she was at the University of Tabriz as Research Assistant at Mechatronics laboratory. As a research assistant at university of Tabriz, she designed and controlled an exoskeleton robot for upper-limb rehabilitation and designed and fabricated the drivers for DC motors of a surgical robot. She is also the co-owner and researcher of Pargar Co., a company for engineering and educational research. She is currently a Research Assistant in the Department of Mechanical Engineering, Washington State University, USA under the supervision of Dr. Swensen. Her research interests are steerable needles, water jet cutting, and medical devices.

John P. Swensen received his M.S. and Ph.D. degrees in Mechanical Engineering from the the Johns Hopkins University, U.S.A, in 2009 and 2012, respectively. He is currently an Assistant Professor in the School of Mechanical and Materials Engineering at Washington State University, and the Director of the Modeling, Motion, and Medical (M3) Robotics Laboratory. The M3 Robotics Laboratory research focuses on research into compliant medical devices, including steerable needles, and other tunably-compliant mechanisms.